# Soft elastomers: a playground for guided waves

Alexandre Delory, Fabrice Lemoult, Maxime Lanoy, Antonin Eddi, Claire Prada

# Soft elastomers: a playground for guided waves

Alexandre Delory,[1,2] Fabrice Lemoult,[1,a] Maxime Lanoy,[1,3] Antonin Eddi,[2] and Claire Prada[1]

[1]*Institut Langevin, ESPCI Paris, Université PSL, CNRS, 75005 Paris, France*

[2]*PMMH, CNRS, ESPCI Paris, Université PSL, Sorbonne Université, Université de Paris, F-75005, Paris, France*

[3]*Laboratoire d'Acoustique de l'Université du Mans (LAUM), CNRS, Le Mans Université, 72085 Le Mans, France*

(Dated: 7 December 2021)

This paper is part of a special issue on Education in Acoustics.

Mechanical waves propagating in soft materials play an important role in physiology. They can be natural such as the cochlear wave in the inner ear of mammalians, or controlled such as in elastography in the context of medical imaging. In a recent study[1], we implemented an experimental tabletop platform that allows direct observation of in-plane guided waves in a soft strip. Here, a detailed description of the set-up and signal processing steps are presented as well as the theoretical framework supporting them. One motivation is to propose a tutorial experiment for visualizing the propagation of guided elastic waves. Last, the versatility of the experimental platform is exploited to illustrate experimentally original features of wave physics such as backward modes, stationary modes and Dirac cones.

[a]fabrice.lemoult@espci.psl.eu

## I. INTRODUCTION

The mechanical behaviour of soft materials plays a crucial role in various physiological processes[2]. For example, the impact of the local stiffness of tissues during their development[3], the stiffening of a tumor cell[4] or the non-linear softening of arteria[5] are customary mechanisms still under investigation. Most biological tissues are *soft* and nearly *incompressible*. Mimicking them requires to fulfil these two mechanical properties. In that regard, elastomers are interesting candidates. Indeed, they cover a wide range of mechanical properties and they can be molded into an infinite variety of shapes. In plastic surgery, silicone rubber have been adopted to reproduce the shapes and mechanical properties of breasts, lips or noses. In the cinema industry, they have become a standard to conceive skin-masks. Nowadays, silicone elastomers seem to be promising materials to build artificial organs (such as vocal folds[6] or hearts[7]), soft robots[8,9] or even baromorph materials[10,11].

Due to their nearly-incompressible nature, these soft materials present interesting dynamical properties involved in the propagation of elastic waves: the longitudinal waves are several orders of magnitude faster than their transverse counterpart ($V_L \gg V_T$). This specificity has enabled the development of transient elastography[12] which is now clinically used for liver cirrhosis[13] or tumor detection[14]. However, elastography is not quantitative when it deals with narrow targets such as artery walls[15–17], the myocardium[18,19], Achilles' tendon[20] or even biofilms[21]. In these geometries, the edges induce guiding phenomena, thus resulting in a different apparent wave velocity. Guided elastic waves are also naturally involved in physiological processes. At the cellular scale, pressure pulses are observed in lipid

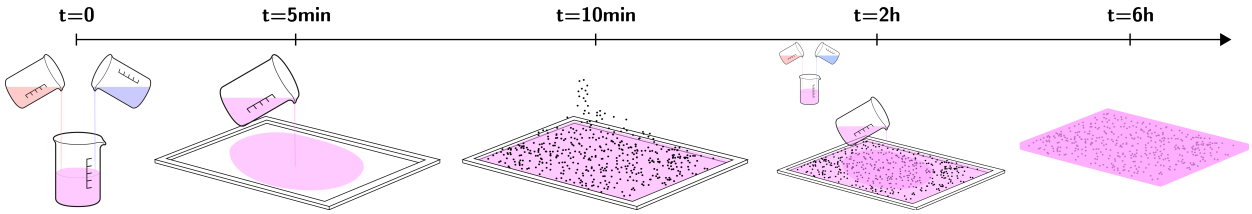


FIG. 1. **Ecoflex® sample preparation** – At time $t = 0$, the monomer and its cross-linking agent are mixed in equal proportions and a first layer is poured in the sample mould. At $t = 10$ min, the sample is sprinkled with black carbon grains dedicated to the displacement tracking. At $t = 2$ hours, a second layer is poured and cures for 6 hours until complete cross-linking.

monolayers[22], and at the macroscopic scale the vocal cords are the support of stationary waves[23]. Another compelling example is the sound transduction operated by the inner ear of mammalians: the *cochlear wave* is a guided mechanical wave that travels along the basilar membrane[24,25].

Although, guiding is a universal wave phenomenon, the case of elastic waves is particularly fascinating: up to three different polarizations can couple at each reflection[26] and at least two distinct wave velocities are involved. Even in a geometry as simple as a plate, elastic guided waves present original properties. These waves have been extensively studied, especially for non-destructive testing applications[27,28]. Under certain conditions, they display unique features such as negative phase velocities[29,30] or zero group velocity (ZGV)[31–34].

This article presents a detailed experimental and theoretical framework for the investigation of the in-plane motion in soft waveguides. First, an experimental platform designed to track the in-plane displacement of a thin plate is proposed. The corresponding theoretical background (Rayleigh-Lamb equation) is exposed. Then, an equivalence between Lamb

modes and the in-plane motion of a thin strip is made. The strip configuration is investigated experimentally as well. Unique wave features such as a backward mode, a zero group velocity point (ZGV) and a Dirac cone in the $k \to 0$ limit are reported[1]. As such, the soft strip appears as an appropriate tutorial configuration to expose the richness of linear elastodynamics. Finally, it is demonstrated how the mode chirality can be exploited to perform selective excitation.

## II. LOW FREQUENCY IN-PLANE GUIDED WAVES IN A SOFT PLATE

This section examines the vibration of a thin plate made of a nearly incompressible material. The experimental procedure is detailed and the measured in-plane fields are presented. Then, the theory supporting these measurements is provided, recalling how the reflections of bulk elastic waves at a free interface lead to the emergence of shear-horizontal guided waves and Lamb waves.

### A. Experiments

The soft plate preparation and the experimental platform is described. Then, the stroboscopic image acquisition and post-processing operations are explained and the resulting in-plane wave-fields are discussed.

### *1. Sample preparation*

All along this article, the selected soft elastomer is the silicone rubber Smooth-On Ecoflex® 00-30, a material that has been widely used in academics in the last few years. As illustrated in figure 1, the rubber is obtained by mixing a monomer (A) and its cross-linking agent (B). The liquid can optionally be vacuumed for air bubbles removal. Next, the mix is poured onto a mould, here consisting of a flat surface with rigid walls forming a 60-centimeter-side square. For a 3-millimeter-thick Ecoflex® plate, one roughly needs 500 mL of each liquid. The mixture is then left for curing at room temperature for several hours until a translucent soft material is obtained. Here, the monomer and its cross-linking agent are mixed in equal quantities. Finally, the shear modulus $\mu$ of the obtained elastomer is approximately 25 kPa.

Anticipating ulterior image processing operations, dark pigments are seeded on the polymer during the curing stage. A good contrast is obtained by using small black carbon powder from a local art shop. The seeding operation can be performed after pouring half of the total volume ($t = 10$ minutes) and before pouring the other half (Fig. 1). In the end, one gets a single layer of pigment located halfway through the plate. In this study, the grain density is approximately of one grain per square millimeter.

### *2. Experimental setup*

The experiment consists in shaking the plate and imaging its in-plane motion. To this end, the soft plate is clamped at its top and bottom extremities into a metallic structure

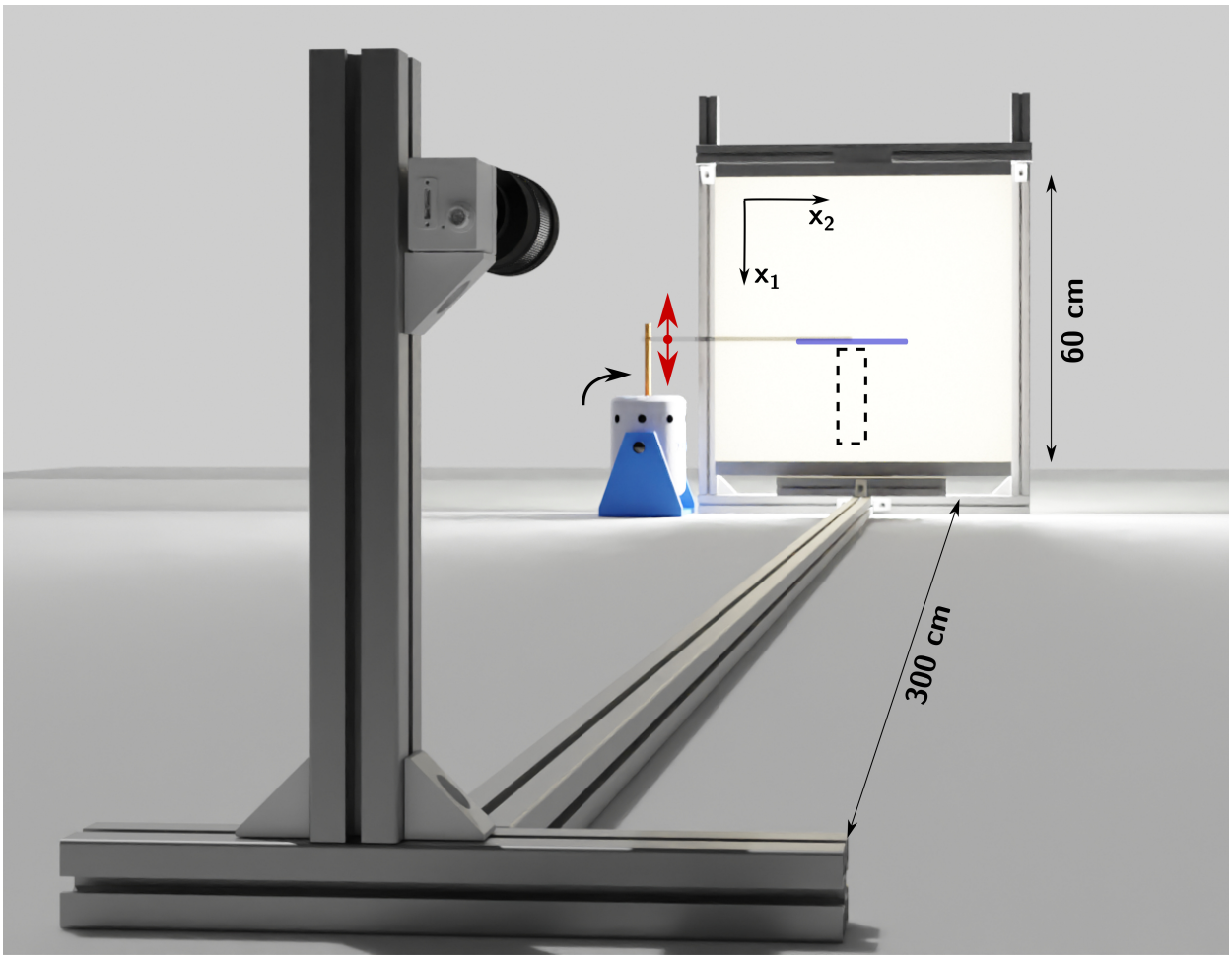


FIG. 2. **Experimental set-up using a line source** – A thin plate of Ecoflex® with dimensions 60 cm x 60 cm x 3 mm is clamped to an adjustable frame on its top and bottom edges, and held in a vertical position. Vibrations are generated by a shaker driven monochromatically. Both the vibration direction and the source orientation can be adjusted in order to excite different polarizations. The experiment is recorded using a CCD camera located 3 m away from the plate.

(Fig. 2) which dimensions can be adjusted in order to avoid static tension, except from gravity.

The excitation is performed by a shaker (Tira Vib 51120), driven by an external arbitrary wave generator (Keysight AWG 33220) which is itself connected to a power amplifier (Tira

Analog Amplifier BAA 500). Typical excitation frequencies span from 1 to 300 Hz. The shaker is connected to a plastic clamp holding a pair of aluminum rods placed on both sides of the soft plate. The two bars pinch the plate over a 30 cm length ensuring the generation of plane-like waves. The shaker and the pinching rods can be rotated to promote specific polarizations. The set-up essentially captures displacements parallel to the plate surface. As a consequence, it is crucial to carefully align the vibration axis of the shaker with the plate to avoid spurious out-of-plane contributions. The motion is captured by a CCD camera (Basler acA4112-20um) with a 4112x3008-pixels sensor (Fig. 2). Note that it is necessary to use a global shutter: all pixels are exposed simultaneously and capture a full snapshot of the scene. A 85-mm zoom lens mounted on the camera and placed 3 meters away from the object provides a clean field of view of roughly 30 centimeters wide square. Narrow angle lenses drastically reduce optical distortions. For an optimal contrast, the system is back-lighted thanks to a wide LED panel placed behind the plate.

### *3. Monochromatic excitation and stroboscopy*

Given the chosen region of interest, the maximum acquisition frame rate of the camera is of roughly 130 Hz. This means that Shannon's criterion is not fulfilled for frequencies higher than 65 Hz. However, in the linear regime, there is no need for a higher speed camera since stroboscopic effect can be exploited. To that end, the acquisition period of the camera $T_{\text{cam}}$ is set slightly greater than the excitation period $T_{\text{excitation}}$, *i.e.* $T_{\text{cam}} = T_{\text{excitation}} + \delta t$. Between two successive snapshots, the field undergoes more than a full oscillation period. Yet, the accumulated phase shift $2\pi\delta t/T_{\text{excitation}}$ remains small. The final movie provides the

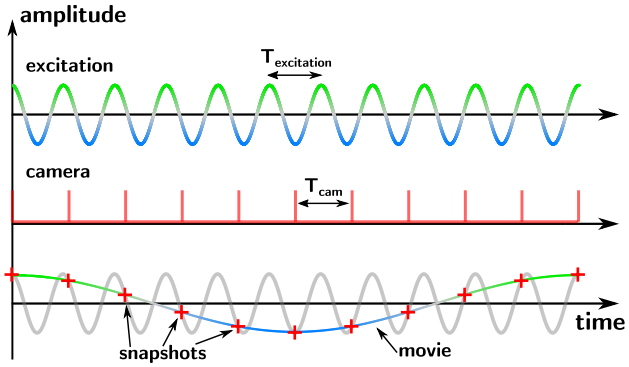


FIG. 3. **Principle of the stroboscopic imaging** – As the recording framerate is lower than the excitation frequency, one full cycle is reconstructed from the measurements, depicted by the red crosses, taken over several cycles of excitation. The sampling rate has to be precisely defined with respect to the driving frequency.

illusion than the successive snapshots belong to a single wave period (sketch on figure 3). We refer to this quantity as the pseudo-period.

For the following post-processing steps, it is preferable to work with a given amount of images per movie. The measurements are performed setting this quantity to $N = 60$ frames over one pseudo-period. This means that the acquisition frame rate has to be determined for each different excitation frequency. If the maximum frame rate of the camera is too low, one can always reduce the sampling frequency by waiting for several excitation periods between successive camera triggers. For example, at 100 Hz, an acquisition sampling rate of precisely 24.8963 Hz would yield to 60 frames regularly spaced within one pseudo-period (the 61st should be the same as the first image), and successive shots occur roughly every 4 periods. Note that the exposure time of the camera should always remain much smaller than the excitation period. The image would be blurred otherwise. Our measurements are

performed with a typical exposure time of 150 $\mu$s. The image quality is seriously hampered above approximately 300 Hz.

In addition to these $N$ frames, a reference image should be captured as the sample is at rest for image processing purposes.

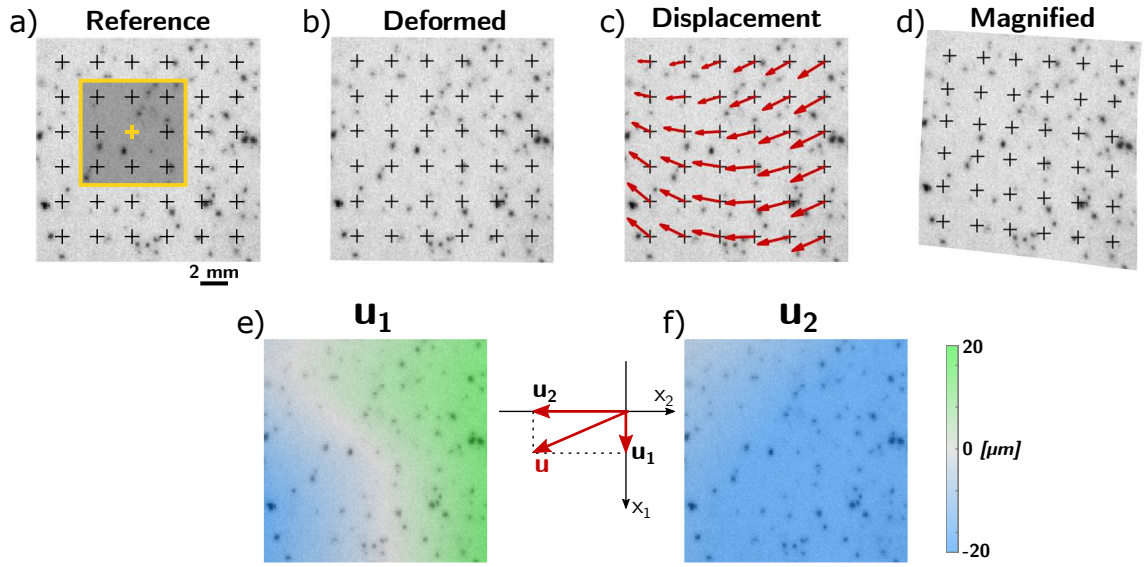


FIG. 4. **Principle of displacement extraction through Digital Image Correlation (DIC) algorithm** – (a) Exemple of a reference image. The black seeds provide a *texture* enabling the DIC analysis. The displacement is computed for each position (crosses) by applying the DIC algorithm over the shaded area. (b) As the shaker is turned on, the image is deformed. The displacements are barely noticeable by eye (typically 10 $\mu$m). The DIC algorithm computes the correlation between the deformed and the reference images. (c) Output of the DIC algorithm. A displacement vector is computed for each macropixel. (d) This displacement is used to build a magnified distorted image where displacements appear clearly. The motion is magnified by a factor 50. (e-f) Vertical (resp. horizontal) displacement maps.

### *4. Extraction of the complex displacement maps*

Next, each of the $N$ frames is compared to the reference thanks to an open source Digital Image Correlation (DIC) algorithm[35,36] which provides the instantaneous displacement (Fig. 4). The correlation is computed on small image regions, called *macropixels*. Each macropixel yields one displacement vector ($u_1$,$u_2$). By repeating the operation for all the macropixels of a single frame, two displacement maps are obtained (Fig. 4e and f). The macropixel size is set manually. It should be large enough to contain several seeds while remaining smaller than the wavelength. Here, macro-pixels extending over 25 pixels $\times$ 25 pixels of the original image are chosen. Sometimes, the algorithm fails to find a realistic solution for a given macropixel. In that case, one can always spatially interpolate the missing information or apply spatial convolution filter to smooth the displacement maps. Note that the DIC algorithm enables sub-pixel resolution. For example, displacements down to 5 $\mu$m are measured when a single image pixel corresponds to 100 $\mu$m on the plate.

The knowledge of the displacement maps gives the opportunity to build magnified version of the deformed image as in Fig 4c. This can be very useful for visualizing the propagation of waves or for teachings. For communication through writing as in this article, a separate representation of the two components of the displacement as a color code (Fig 4d and e) is preferred.

At this stage, for a given excitation pulsation $\omega$, a series of $N$ displacement matrices $\mathbf{u}^{(n)}(\mathbf{r})$ are obtained, where $n \in [0, N-1]$ refers to the frame index. From this series, the

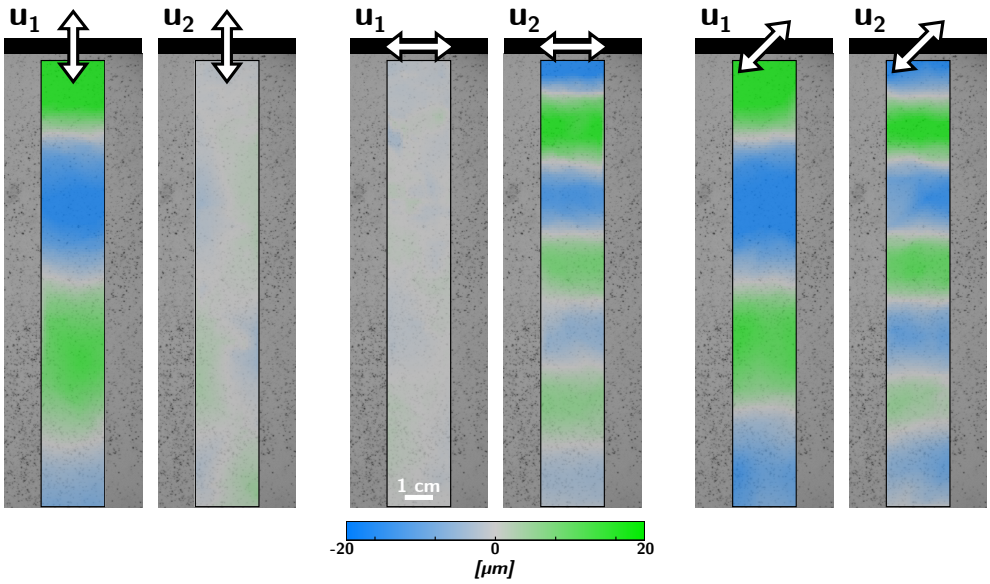


FIG. 5. **Measurement of in-plane waves in a soft plate** – Displacement fields in both vertical ($u_1$) and horizontal ($u_2$) directions measured for three excitation directions with a forcing frequency $f = 120$ Hz. The source oscillates vertically (left), horizontally (middle) or at 45° (right). The colorbar indicates the magnitude of the in-plane displacements in the elastic plate.

complex monochromatic displacement is computed as following:

$$\mathbf{u}(\mathbf{r},\omega) = \frac{1}{N}\sum_{n=0}^{N-1} \mathbf{u}^{(n)}(\mathbf{r}) e^{\frac{2in\pi}{N}} \tag{1}$$

The data contained in 60 memory-consuming frames of thousands of pixels has been reduced to the knowledge of a single complex matrix of a few hundreds points.

### *5. Measured in-plane modes*

With the set-up of figure 2, field maps are acquired in an area of 17 cm × 2.4 cm below the clamp (dashed area in the same figure). Figure 5 gathers the real parts of the extracted displacements for an excitation frequency of 120 Hz. Three different vibration orientations

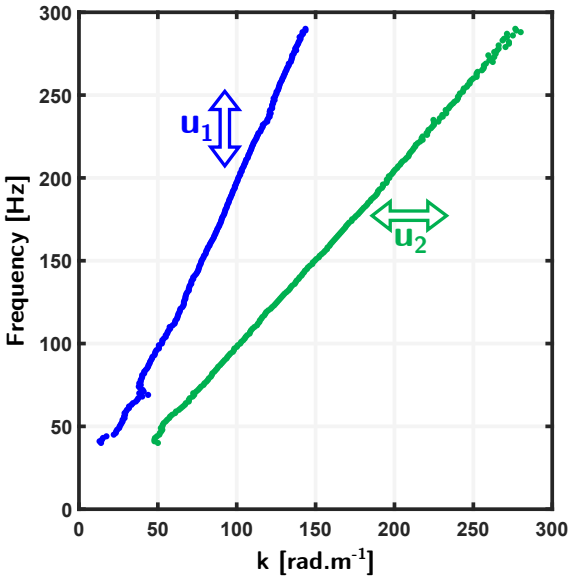


FIG. 6. **Experimental dispersion curves of in-plane modes in a 3-mm-thick soft plate** – A vertically polarized (blue) and a horizontally polarized (green) non dispersive modes are retrieved. The vertically polarized mode propagates twice faster than the horizontally polarized one.

(vertical, horizontal and 45°) are investigated while the 30-cm-wide clamp is maintained horizontal.

In the left part of the figure 5, for which the vibration is vertical, $u_2$ cancels everywhere in the measured area: the motion is purely vertical (*ie.* aligned with $x_1$). Also, $u_1$ exhibits a periodic pattern along the $x_1$ direction and a flat profile along $x_2$, and the phase travels toward the bottom (not shown here). This measurement corresponds to a plane wave-like pattern (with a wavelength $\lambda$ of roughly 10 cm) with both the displacement and the wavevector being parallel to $x_1$. The plate thus supports an in-plane guided elastic wave that we can qualify as longitudinal. Similarly, the horizontal excitation along $x_2$ of the clamp (middle column in figure 5) generates a plane wave-like propagation with a polarization parallel to

$x_2$, that can be qualified as a transverse wave. Interestingly, its wavelength is exactly half the wavelength of its longitudinal counterpart. The versatility of this experimental platform is highlighted in the right panel of figure 5. Indeed, instead of selectively exciting each type of plane wave, a motion of the clamp along a 45° tilted direction excites simultaneously the two waves: with one measurement several modes can be retrieved.

Finally, a systematic extraction of the two aforementioned plane waves for frequencies ranging from 50 to roughly 300 Hz is performed. For each frequency, the maps are averaged along $x_2$, meaning projected unto a plane wave. Then, for each solution a wavenumber (an inverse measure of the wavelength) along the $x_1$ direction is obtained by keeping the maximum of the spatial Fourier transform of the profile along $x_1$. This way, a dispersion diagram (*i.e.* frequency as a function of wavenumber) is constructed for the two polarizations in figure 6. Both the dispersion curves appear to be straight lines passing through the origin. It corresponds to a non-dispersive propagation, that is to say a propagation at a constant phase velocity. The factor 2 between the wavelengths here manifests as a factor 2 between the two slopes: the longitudinal mode travels twice faster than the transverse one.

In the higher part of the measured frequency range the experimental points slightly move off the linear behaviour. The rheology of the polymer is at the origin of this deviation, as explained in section III C, but it remains anecdotal at this stage.

## B. Theoretical background

These observations can be explained thanks to a simple theoretical description. The propagation of elastic waves in isotropic solids is a well documented topic. Comprehensive developments can be found in the following textbooks[26,37].

### *1. Bulk waves*

The elastodynamics of a homogeneous isotropic solid requires the knowledge of, at least, two elastic moduli. For historical reasons, people usually refer to the Lamé constants $\lambda$ and $\mu$[1]. But, these two constants can be substituted by any other couple of elastic coefficients such as the Young modulus $E$, the bulk modulus $K$ or the Poisson's ratio $\nu$. The case of nearly incompressible media corresponds to the limit when $\nu \to \frac{1}{2}$. Knowing that $\nu = \frac{\lambda}{2(\lambda+\mu)}$, this amounts to $\lambda \gg \mu$ in terms of the Lamé constants.

By combining the Newton's law of motion and the Hooke's law applied to an infinitesimal volume, one finds that the local displacement field $\mathbf{u}(\mathbf{r}, t)$ obeys the following vector wave equation:

$$\rho \frac{\partial^2 \mathbf{u}}{\partial t^2} = (\lambda + \mu)\nabla(\nabla.\mathbf{u}) + \mu \Delta \mathbf{u} \tag{2}$$

where $\rho$ stands for the mass density of the solid and $\nabla$ is the gradient operator. In this equation the three components of the displacement field are coupled. In order to decouple the equations it is common to introduce the scalar potential $\phi$ and the vector potential $\mathbf{\Psi}$

as:

$$\mathbf{u} = \nabla\phi + \nabla \times \mathbf{\Psi} \tag{3}$$

The component $\nabla\phi$ corresponds to an irrotational vector field while the component $\nabla \times \mathbf{\Psi}$ is associated to a divergence free field, that is a deformation without any volume change. These two potentials are independent and satisfy the following decoupled wave equations:

$$\frac{\partial^2\phi}{\partial t^2} - \frac{\lambda + 2\mu}{\rho}\Delta\phi = 0 \tag{4}$$

$$\frac{\partial^2\mathbf{\Psi}}{\partial t^2} - \frac{\mu}{\rho}\Delta\mathbf{\Psi} = 0 \tag{5}$$

These d'Alembert equations confirm the propagation of two different types of waves with distinct polarizations and velocities. On the one hand, equation (4) corresponds to a longitudinal wave propagating at velocity $V_L = \sqrt{(\lambda + 2\mu)/\rho}$ and with a displacement parallel to the propagation direction. On the other hand, equation (5) stands for transverse (or shear) waves propagating at the velocity $V_T = \sqrt{\mu/\rho}$ with displacements perpendicular to the propagation direction. Ecoflex® 00-30 has a measured longitudinal velocity of approximately 1000 m/s while the shear wave velocity is about 5 m/s. This high contrast between the two velocities ($V_L \gg V_T$) confirms its incompressible nature as:

$$\nu = \frac{{V_L}^2 - 2{V_T}^2}{2\left({V_L}^2 - {V_T}^2\right)} \approx \frac{1}{2} \tag{6}$$

### *2. Reflection at a free interface*

The problem of reflection at an interface reveals the richness of the elastodynamics. Consider an incident plane wave propagating in the plane $(x_1, x_3)$ impinging on a medium

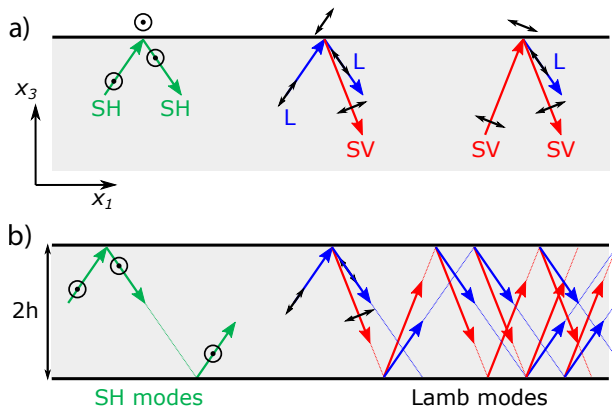


FIG. 7. **Reflection at a free interface and mode coupling** – (a) Reflection of a shear horizontal ($SH$) wave at an interface does not generate out-of-plane displacements while longitudinal ($L$) and shear vertical ($SV$) waves couple. (b) When multiple reflections occur, $SH$ waves remain independent while $L$ and $SV$ waves couple leading to a new family of modes: namely Lamb waves.

interface at $x_3 = 0$ (Fig. 7a). As elastic waves have three polarizations, the reflection at the interface gives rise to three different plane waves. However, the so-called shear horizontal ($SH$) wave with displacement along $x_2$ ($u_1 = u_3 = 0$) can only be generated as a reflection of a shear horizontal wave as sketched in figure 7a. On the contrary, longitudinal and shear vertical waves (by opposition to the shear horizontal ones) with displacements in the plane $(x_1, x_3)$ are coupled through reflections at the interface.

Reflection at one interface is the entrance door to more complicated wave phenomena, and notably waveguiding which occurs as a second interface, parallel to the first one, is added. As sketched in figure 7b, the separation between the $SH$ waves and the two others remains valid in this configuration. The two following sections describe the two families of modes that can propagate in a soft plate of thickness $2h$.

### 3. SH guided waves

The case of shear-horizontal guided waves is relatively simple because its dispersion curves map those of the well known acoustic waveguides. Indeed, as all displacements occur along the $x_2$ direction, the problem becomes a scalar wave problem. Applying the translational invariance along the $x_1$ direction one seeks for monochromatic solutions of the form:

$$\mathbf{u}(\mathbf{r},\omega) = \begin{pmatrix} 0 \\ u_2(x_3,\omega) \\ 0 \end{pmatrix} e^{ikx_1} \tag{7}$$

Assuming that the interfaces at $x_3 = \pm h$ are free to move, the stress component $T_{23}$ at these interfaces vanishes:

$$T_{23}(x_3 = \pm h) = \mu \left.\frac{\partial u_2}{\partial x_3}\right|_{x_3=\pm h} = 0 \tag{8}$$

Solving the wave equation (2) for shear waves together with these boundary conditions provides the solutions for the guided shear horizontal waves inside the plate:

$$u_2(x_3,\omega) = C\cos\left(\frac{n\pi}{2h}(x_3 - h)\right) \tag{9}$$

where $C$ is a scalar constant. And the dispersion relation simply writes:

$$k^2 = \left(\frac{\omega}{V_T}\right)^2 - \left(\frac{n\pi}{2h}\right)^2 \tag{10}$$

Such a dispersion relation (figure 8) exhibits a non-dispersive mode, denoted $SH_0$, propagating at all frequencies at the shear velocity $V_T$, as well as dispersive propagating modes above their respective cut-off frequencies of $f_{c_n} = nV_T/4h$. For a thickness of 3 mm and

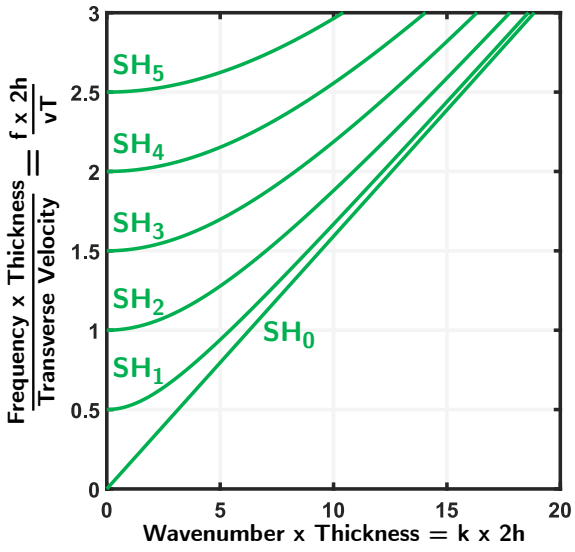


FIG. 8. **Theoretical dispersion curves of SH waves** – The $SH_0$ mode is non dispersive with a velocity $V_T$ while higher modes appear at cut-off frequencies corresponding to every multiple of $\frac{V_T}{4h}$.

a shear velocity of roughly 5 m/s, the first cut-off frequency is at 833 Hz, far above the measured frequencies in the experimental part. Thus, the displacement field displayed in figure 5 polarized along $x_2$ corresponds to this $SH_0$ mode. This transverse mode has already experimentally demonstrated its non-dispersive nature in figure 6 (green line).

### *4. Lamb waves*

Due to the coupling at each reflection, the case of longitudinal waves and shear vertical ones is more complicated. However, the calculation steps to establish the dispersion relation and the solutions remain similar. Here, it is preferable to start back from the scalar and vector potentials $\phi$ and $\mathbf{\Psi}$. Applying some geometrical arguments, their expressions can be simplified. First, the invariance by translation along $x_1$ implies the dependence on $x_1$

to be on the form $e^{ikx_1}$. Second, the component of the displacement $u_2$ is zero and the other components should not depend on $x_2$. Third, the plane $x_3 = 0$ is a symmetry plane, so the solutions should either be symmetric or anti-symmetric. Considering all of these simplifications and solving the wave equations (4) and (5), their analytical formulations write:

$$\begin{cases} \phi(\mathbf{r},\omega) &= \phi_0 \cos(px_3+\alpha)e^{ikx_1} \\ \\ \mathbf{\Psi}(\mathbf{r},\omega) &= \psi_2 \sin(qx_3+\alpha)e^{ikx_1}\mathbf{x_2} \end{cases} \tag{11}$$

with $p^2 = (\omega/V_L)^2 - k^2$ and $q^2 = (\omega/V_T)^2 - k^2$. Symmetrical solutions correspond to $\alpha = 0$ and anti-symmetrical ones to $\alpha = \pi/2$. From these potentials, the displacements now write:

$$\mathbf{u}(\mathbf{r},\omega) = \begin{pmatrix} u_1(x_3,\omega) \\ \\ 0 \\ \\ u_3(x_3,\omega) \end{pmatrix} e^{ikx_1} \tag{12}$$

with the two non-zero components being:

$$\begin{cases} u_1(x_3,\omega) &= ik\phi_0 \cos(px_3+\alpha) - q\psi_2 \cos(qx_3+\alpha) \\ \\ u_3(x_3,\omega) &= -p\phi_0 \sin(px_3+\alpha) + ik\psi_2 \sin(qx_3+\alpha) \end{cases} \tag{13}$$

The dispersion relation of these modes is deduced from the boundary conditions. Assuming free boundaries at both interfaces $x_3 = \pm h$ the stresses $T_{13}$ and $T_{33}$ must cancel, which imply:

$$\begin{cases} (k^2-q^2)\phi_0 \cos(ph+\alpha) &= 2ikq\psi_2 \cos(qh+\alpha) \\ \\ (k^2-q^2)\psi_2 \sin(qh+\alpha) &= 2ikp\phi_0 \sin(ph+\alpha) \end{cases} \tag{14}$$

Non-trivial solutions for $\phi_0$ and $\psi_2$ are found when the determinant of this system vanishes. Under these circumstances, $u_1$ and $u_3$ write with a single scalar coefficient $C$ as:

$$\begin{cases} u_1(x_3,\omega) = Cq\left[\frac{2ik}{k^2-q^2}\cos(qh+\alpha)\cos(px_3+\alpha)\right. \\ \qquad\qquad \left. +\cos(ph+\alpha)\cos(qx_3+\alpha)\right] \\ u_3(x_3,\omega) = iCk\left[\frac{2ip}{k^2-q^2}\cos(qh+\alpha)\sin(px_3+\alpha)\right. \\ \qquad\qquad \left. +\cos(ph+\alpha)\sin(qx_3+\alpha)\right] \end{cases} \tag{15}$$

And the dispersion relation, known as the "Rayleigh-Lamb equation", writes:

$$(k^2-q^2)^2\sin(qh+\alpha)\cos(ph+\alpha) = 4k^2pq\sin(ph+\alpha)\cos(qh+\alpha) \tag{16}$$

Unfortunately the Rayleigh-Lamb equation (16) does not have general analytical solutions and it must be solved numerically. A Muller algorithm[39] is used to find the roots of this equation for the nearly-incompressible soft plate considered here. The dispersion curves displayed in figure 9 highlight the families of symmetric and anti-symmetric modes. Below the first cut-off frequency of $V_T/4h \approx 833$ Hz, only two modes exist: the anti-symmetric $A_0$ and the symmetric $S_0$ modes. While $A_0$ dispersion curve is parabolic in the low frequency limit, the $S_0$ mode is non-dispersive.

The displacements of these modes given by equations (15) can also be simplified in the limit $kh \to 0$. For $A_0$, one finds:

$$\begin{cases} u_1(x_3,\omega) = iC'kx_3 + o(k) \\ u_3(x_3,\omega) = C' + o(k) \end{cases} \tag{17}$$

where the new constant $C'$ has been introduced without losing generality. The displacement $u_3$ is homogeneous across the thickness, and the displacement $u_1$ is relatively negligible

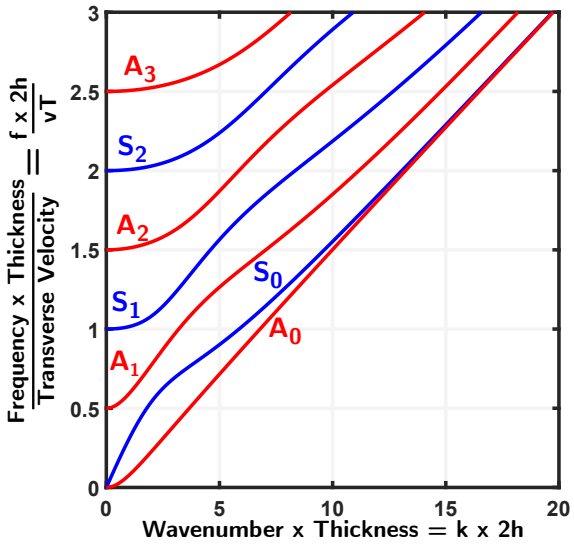


FIG. 9. **Theoretical dispersion curves of Lamb waves in a nearly incompressible material** – Dispersion curves of the symmetric (blue) and anti-symmetric (red) Lamb modes. In the low frequency range, the $S_0$ mode is non dispersive with a velocity $V_P = 2V_T$ while the $A_0$ dispersion curve is parabolic. Higher modes exhibit cut-off frequencies every multiple of $\frac{V_T}{4h}$.

($kx_3 \to 0$). This mode, generally called flexural mode, is therefore mostly a transverse vertical mode. It is not measured in the previous experiment since the shaker is aligned in order to avoid out-of-plane displacements.

Taking the limit for the $S_0$ mode gives:

$$\begin{cases} u_1(x_3,\omega) &= C' + o(k) \\ u_3(x_3,\omega) &= iC'kx_3 + o(k) \end{cases} \tag{18}$$

This time, the displacement $u_1$ is homogeneous across the plate and is far greater than the displacement $u_3$. In a sense, in this low frequency limit and long wavelength approximation (compared to the thickness) the $S_0$ mode is seen as a longitudinal mode. Its phase velocity,

known as the plate velocity, is given by:

$$V_P = 2V_T\sqrt{1-\left(\frac{V_T}{V_L}\right)^2} = \sqrt{\frac{2}{1-\nu}}V_T \tag{19}$$

The surprising feature is that, in the incompressible limit, the phase velocity of $S_0$ simplifies to $V_P = 2V_T$. It is thus independent of the longitudinal velocity $V_L$ despite its apparent longitudinal polarization. This mode corresponds to the measured displacement $u_1$ presented in figure 5, which has twice the wavelength of the $SH_0$ mode. This analytical derivation now explains the ratio of 2 observed in the experimental dispersion curves in figure 6.

## III. IN-PLANE GUIDED WAVES IN A SOFT STRIP

In this section, a different geometry is considered: a thin rectangular waveguide made of the same nearly incompressible material. It is made by a parallel cutting of the previous plate. First, an analogy is made between this geometry and the plate geometry already described. Notably, the dispersion of in-plane modes propagating in this strip is shown to be similar to the one of Lamb waves propagating in an isotropic plate with a longitudinal wave velocity being exactly twice the shear wave velocity. Then, the experimental results already reported in Lanoy *et al.*[1] are presented. The procedure used to separate the modes in order to obtain their profiles as well as their phase velocities is thoroughly described.

### A. Theoretical framework

The theory of elastic modes propagating in rectangular waveguide is not straightforward. As this geometry involves three coupled polarizations, obtaining the full dispersion diagram

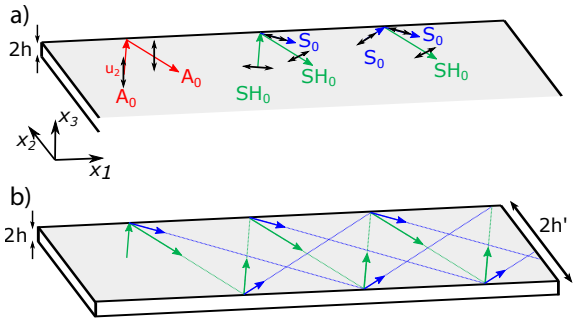


FIG. 10. **Mode coupling in a strip** – (a) The edge reflection of the $A_0$ mode only generates $A_0$ while $S_0$ and $SH_0$ waves couple. (b) Multiple reflections lead to $S_0$ and $SH_0$ in-plane mode coupling in a similar manner to shear and longitudinal waves couple in an infinite plate.

can be challenging[40]. Thanks to the Rayleigh-Lamb approximation[41,42], the problem drastically simplifies as one deals with the in-plane modes of a strip with a large aspect ratio. This part treats this problem in the specific case of a soft solid.

### *1. Analogy with Lamb waves in a plate*

As explained in the previous section, at low frequencies, only three modes propagate in a plate: the first shear horizontal mode $SH_0$ (Fig. 8), and the symmetric $S_0$ and anti-symmetric $A_0$ Lamb modes (Fig. 9). They have uniform profiles across the plate and can roughly be considered as linearly polarized. In particular, $S_0$ can be seen as a pseudo-longitudinal wave propagating at the constant "plate" velocity $V_P$. Besides, as shown in equation (13), for nearly incompressible materials the plate velocity is $V_P = 2V_T$.

These observations enable to build an analogy between Lamb waves in a plate and in-plane guided waves in a thin strip as sketched in figure 10. The polarization of $A_0$ is essentially parallel to the strip edge. As a consequence, adding a second edge to form a ribbon of width

309 $2h'$ (figure 10b), $SH_0$ and $S_0$ give rise to guided waves whose displacements stay in the main
310 plane of the ribbon. They are called in-plane guided modes. As shown in the section III of
311 reference[41], this coupling is similar to the one of shear and compression bulk waves in a plate.
312 In other words, the low frequency dispersion diagram for in-plane guided waves in a strip is
313 equivalent to the one for guided waves in a plate. In the following descriptions, the symbol
314 " $'$ " will be added to the notations when dealing with the strip configuration. Typically,
315 the plate thickness $2h$ is replaced by the strip width $2h'$, the longitudinal wave propagating
316 at $V_L$ is replaced by the linearly polarized in-plane wave $S_0$ propagating at velocity $V_P$ (that
317 is $V_L' = V_P$), and the $SV$ wave propagating at $V_T$ is replaced by the transversely polarized
318 in-plane wave $SH_0$ propagating at $V_T$ (that is $V_T' = V_T$). This amounts to solving the Lamb
319 problem for a material of equivalent Poisson's ratio:

$$\nu' = \frac{\nu}{1+\nu} \tag{20}$$

320 where $\nu$ is the Poisson's ratio of the strip material. For incompressible materials, the equiv-
321 alent Poisson's ratio is $\nu' = 1/3$, and the knowledge of $V_T$ is sufficient to obtain the full
322 dispersion diagram of the in-plane guided waves in the low frequency range.

323 ***2. Dispersion relation: key physical features***

324 The dispersion curves of the in-plane modes propagating in a soft strip are thus obtained
325 by finding the roots of the Rayleigh-Lamb equations (16). The solutions are displayed in
326 figure 11 in normalized units. Several interesting properties deserve to be highlighted.

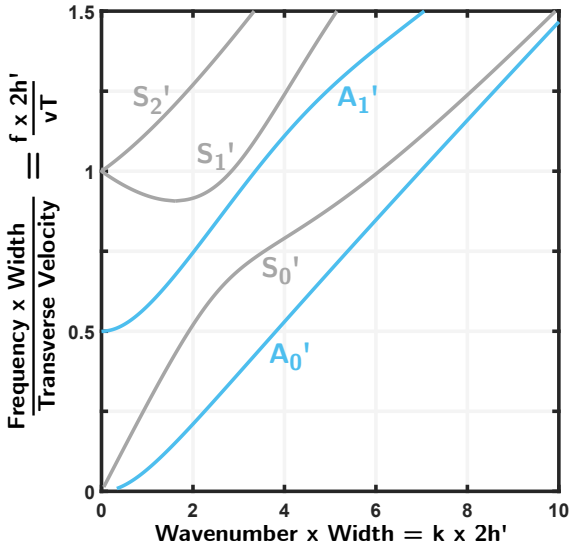


FIG. 11. **Theoretical dispersion curves of in-plane modes in a soft strip** – Dispersion curves of symmetric (gray and labeled $S'$) and anti-symmetric (blue, $A'$) modes without damping. From these curves, one can extract the bar velocity (mode $S'_0$ at low frequencies), evidence a Zero Group Velocity point ($S'_1$) and a backward branch, as well as a Dirac cone with a finite group velocity at $k = 0$ (at $f = V_T/2h'$)

*a. Bar velocity.* The first symmetrical mode, denoted $S'_0$, is non dispersive for frequencies below the first cut-off frequency. Similarly, to the first symmetric $S_0$ Lamb mode, $S'_0$ can be seen as a longitudinally polarized mode since it corresponds to a pure compression mode of the ribbon. Its phase velocity can be calculated as a pseudo-plate velocity $V'_P$. This velocity deduced from equation (19) has a remarkably simple formulation:

$$V'_P = \sqrt{\frac{2}{1-\nu'}} V_T = \sqrt{2(1+\nu)} V_T \tag{21}$$

In the incompressible limit, it simplifies to $V'_P = \sqrt{3} V_T$. As a consequence, $S'_0$ roughly travels at the transverse velocity, despite being longitudinally polarized mode. This is all the more

striking as, in the incompressible limit, the transverse velocity happens to be several orders of magnitude smaller than the longitudinal velocity.

Furthermore, $V'_P$ also corresponds to the well known bar velocity, associated to the propagation of compression waves along any bar or rod regardless of their cross-section. It can be obtained from an intuitive reasoning. As it corresponds to a longitudinal extension of the waveguide, the relevant elastic modulus is the Young's modulus $E$ and the associated velocity is $\sqrt{E/\rho}$. After injecting the expression $E = 2\,(1+\nu)\,\mu$, one immediately gets equation (21). For a soft material, the Young's modulus simplifies to $E = 3\mu$ and the bar velocity again appears independent of $V_L$.

*b. Zero Group Velocity and Negative Phase Velocity.* Like for Lamb modes, the second symmetrical mode $S'_1$ has a remarkable behavior. Indeed, the corresponding branch exhibits a local minimum for a finite wavenumber. At this specific location, the group velocity $V_g = \mathrm{d}\omega/\mathrm{d}k$ vanishes. This is the signature of a Zero Group Velocity (ZGV) point. For small wave numbers, the $S'_1$ branch has a negative slope. This indicates that the group velocity is opposite to the phase velocity. Causality imposes that the energy travels from the source to the receiver. As a consequence the group velocity should always remain positive. In practice, this negative slope section cannot be measured. The experimentalist rather accesses its symmetric with respect to the $k=0$ axis. This is further discussed in the following sections.

*c. Dirac cones: finite group velocity at $k \to 0$.* In the small wavenumber limit ($k \to 0$), the branches of the dispersion curve become horizontal (for example the Lamb modes in the plate of figure 9). The dispersion relation $\omega(k)$ is quadratic around the cut-off pulsation

$\omega_c$. As shown by Mindlin[43], this expansion does not hold for Lamb modes when there is a coincidence between a shear and a longitudinal cut-off frequency of the same symmetry. In these particular cases, the dispersion law is linear in the limit $k \to 0$ and writes to the first order in $k$ as:

$$\omega(k) = \omega_c + V_g k + o(k) \tag{22}$$

Such coincidences occur for symmetrical modes $S_{2m+1}$ and $S_{2n}$, when the bulk velocity ratio $V_L/V_T$ is equal to $2n/(2m+1)$, and for anti-symmetrical modes $A_{2m+1}$ and $A_{2n}$ when $V_L/V_T = (2m+1)/2n$. For example, recent experiments conducted in a cooled aluminum plate ($V_L/V_T = 2$) by Stobbe and Murray[44] illustrate this linear dispersion near $k = 0$. For modes $S_1$ and $S_2$, the linear slopes of the curve $\omega(k)$ can be derived by developing equation (16) to the first order and it was found[43] to be $V_g = \pm 2V_T/\pi$.

The Lamb wave approximation for in-plane modes in a thin soft strip (*ie.* $\nu' = 1/3$) reveals a coincidence frequency for the symmetrical modes $S'_1, S'_2$. As a result these two modes cross linearly at the normalized frequency $f2h'/V_T = 1$ in figure 11. This linear crossing is also referred to as a Dirac cone[45,46].

*d. Displacement near the Dirac cone.* From equations (15) one can determine the displacements close to the cut off frequencies. For the strip configuration, index 3 must be replaced by 2, $h$ by $h'$ and $p$ by $p'$ such that $p'^2 = (\omega/V_P)^2 - k^2$. The Taylor expansion of coefficients $p'$ and $q$ near the value $k = 0$ are:

$$\begin{cases} p' &= \frac{\pi}{2h'} + \frac{V_g}{2V_T} k + o(k) \\ q &= \frac{\pi}{h'} + \frac{V_g}{V_T} k + o(k) \end{cases} \tag{23}$$

Using $s$ as the sign of the group velocity, the Taylor expansion of the displacement components at the coordinate point $x_2$ becomes:

$$\begin{cases} u_1(x_2,\omega) &= C\frac{\pi}{h'}\cos\left(\frac{\pi}{h'}x_2\right) + O(k) \\ u_2(x_2,\omega) &= -isC\frac{\pi}{h'}\sin\left(\frac{\pi}{2h'}x_2\right) + O(k) \end{cases}$$

For ordinary cut-offs, the displacement is either purely longitudinal or purely transverse. Instead, when there is a coincidence, both polarizations are involved. The factor $i$ between the two components denotes an elliptical polarization. At the specific location $x_2 = \pm h'$, the polarization becomes purely circular. The factor $s$ indicates that modes of opposite group velocities are associated to opposite rotation directions.

### B. Measurements in a soft strip

The soft plate is now replaced with a soft strip. The edges are cut using a laser cutter (Trotec Engraver Speedy 100). The final strip is 60 cm long, 3 mm thick and its width is $h' = 4$ cm. The wide source is replaced with a point-like clamp, obtained by putting two half spheres in contact. The clamp is slightly off-centered and vibrated vertically in order to feed the system in a non-selective manner. A picture of the setup[1] is reported in figure 12.

Here again, the strip is shaken monochromatically for frequencies ranging from 1 to 200 Hz. The camera captures the motion by following the stroboscopic sketch pictured in figure 3. Finally, the displacement field is extracted by applying the DIC algorithm to the successive snapshots. For example, the obtained field maps at 110 Hz are represented in figure 13. The wave pattern is rather different from the one obtained in the plate experiment.

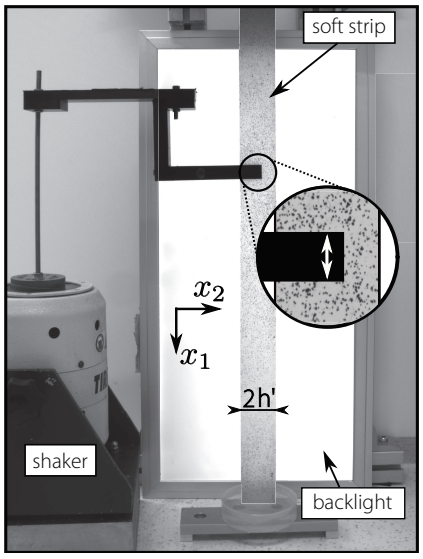


FIG. 12. **Experimental set-up using a point-like source** – A thin strip ($L = 60$ cm, $2h' = 40$ mm, $2h = 3$ mm) is held vertically. A shaker excites in-plane displacements propagating in the strip.

This comes from a superposition between several modes with different propagation constants and spatial profiles.

Separating and identifying them requires two additional post-processing steps schematized in figure 13. First, the symmetrical and anti-symmetrical parts are extracted by respectively summing or subtracting the displacement map with its flipped (along the $x_2$ direction) counterpart. The concatenation of these field maps yields to the construction of two bigger matrices $\mathbf{U}$ (top of Fig. 13), one for each type of symmetry. Then, a Singular Value Decomposition (SVD) is performed on each matrix. This amounts to the following matrix decomposition:

$$\mathbf{U} = \mathbf{V}\Sigma\mathbf{W} \tag{24}$$

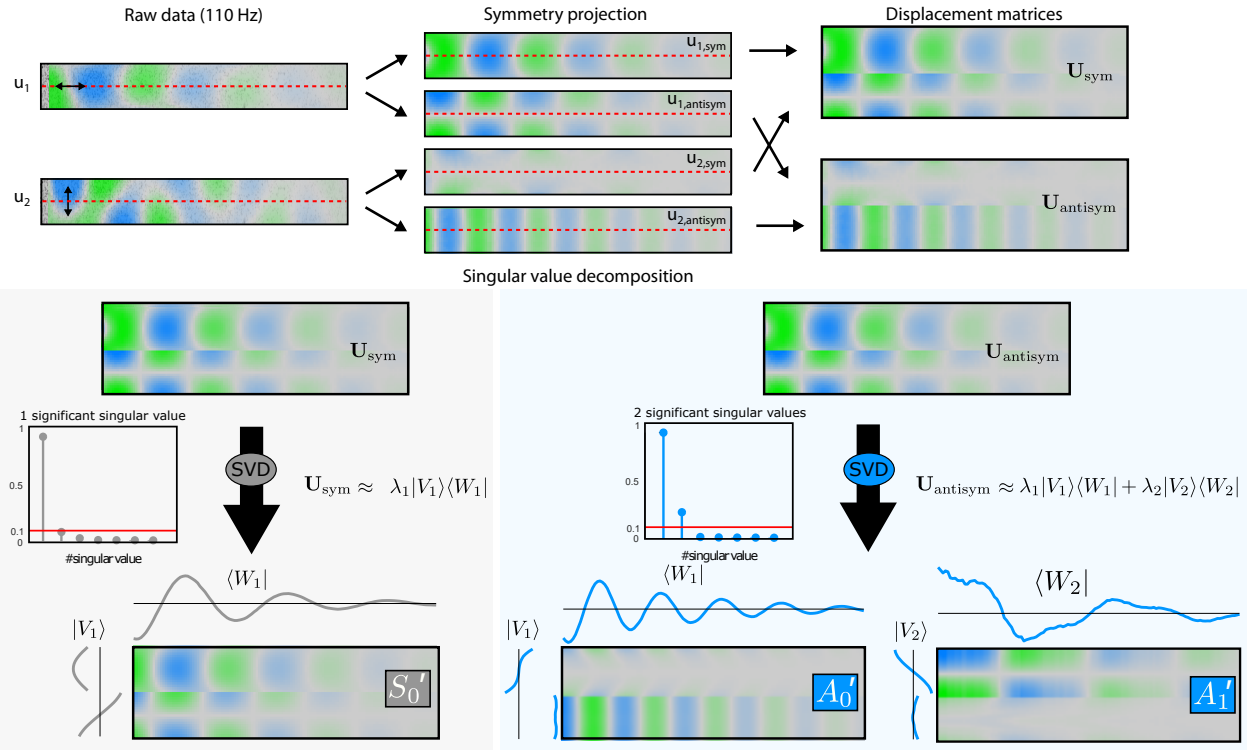


FIG. 13. **Mode separation via Singular Value Decomposition (SVD)** – The in-plane displacement components $u_1$ and $u_2$ (top left) are projected onto their symmetrical and anti-symmetrical parts (top right). Data are then concatenated into a single complex matrix $U_{\text{sym}}$ (resp. $U_{\text{antisym}}$) on which the SVD is directly applied. After extracting the most significant modes (singular values above a 10% threshold), we obtain (here at 110 Hz) one symmetrical ($S_0'$) and two anti-symmetrical ($A_0'$ and $A_1'$) modes.

where $\mathbf{V}$ and $\mathbf{W}$ are unitary matrices providing the displacement profile along $x_2$ and $x_1$ respectively and $\mathbf{\Sigma}$ is a diagonal matrix providing the singular values (*i.e.* the mode prominence in the overall measurement). As a selection criterion, all modes associated with singular values of at least 10% of the maximum singular value are considered as meaningful. The other ones are rejected. At 110 Hz (see figure 13), three modes have a relevant contribution:

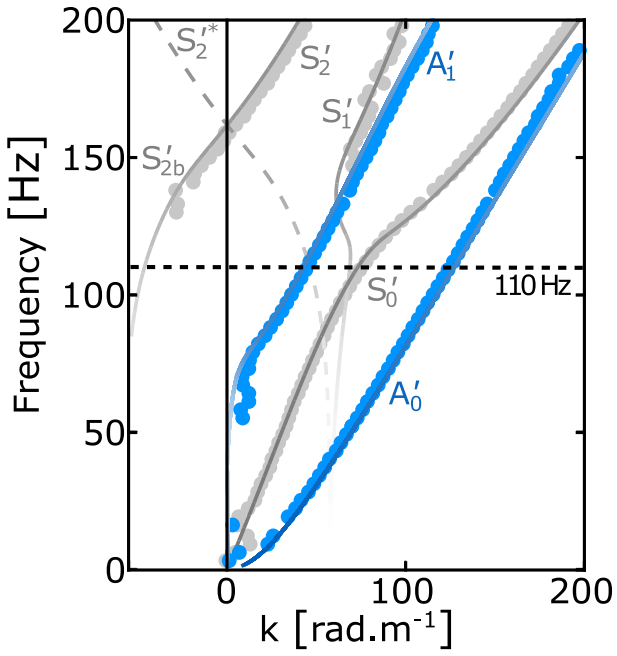


FIG. 14. **Dispersion curves of in-plane modes in a free strip ($2h' = 39$ mm)** – Experimental (symbols) and theoretical (lines) dispersion curves with damping (the more transparent the curve the more attenuated the mode). The Dirac cone (linear crossing of the $k = 0$ axis) and the backward modes (negative wavenumbers) are unambiguously evidenced, while the ZGV point has disappeared. The dashed line denoted by a "*" is drawn by symmetry and corresponds to a mode propagating in the direction $-\mathbf{x_1}$.

two symmetrical modes and one anti-symmetrical. Since **W** gives the displacement along the propagation direction, its Fourier transform yields the wavenumbers of the contributing modes.

These steps are repeated for all frequencies and the dispersion curves represented as symbols in figure 14 are constructed. As stated earlier, in the experiments, one measures negative phase velocities rather than negative group velocities. This is the reason why the horizontal axis covers negative values.

### C. Discussion

Overall experimental dispersion curves in figure 14 relatively resembles the theoretical one in figure 11 and most of the discussed key features are visible. Indeed, the bar velocity of the strip (mode $S'_0$ at low frequency) matches the expected value of $\sqrt{3}V_T$ (where $V_T$ is deduced from the $SH_0$ velocity measured in the plate of figure 5). At 150 Hz, $S'_2$ crosses the axis $k = 0$ with a linear slope: this is a Dirac cone. Note that, below the Dirac frequency, the measured points have negative wave-numbers : this is a signature of a negative phase velocity. The continuity in the measured points naturally leads to label this backward branch $S'_{2b}$ ("b" for backward). This may appear in contradiction with the dispersion curves for lossless material shown in Fig. 11 where the backward mode belongs to the $S'_1$ branch. However, when the complex wave numbers are displayed as done by Mindlin for Lamb modes[47], it clearly appears that the backward branch is connected to $S'_2$ mode even when the cone does not exist[43], thus this notation is adopted in several papers[30,33,42,48].

However, there are two main differences between the theory in figure 11 and the experiment. First, the Dirac cone should be at exactly $2h'/V_T$ but it does not match the value found from the bar velocity neither the value deduced from the asymptotic behaviour at high frequencies of $A'_0$ and $S'_0$. Second, the ZGV point is not visible in the experiment. These two differences both originate from the complex rheology of the elastomer[2].

It is independently measured with a conventional rheometer (Anton-Paar MCR501) which operates in the plate-plate configuration. To this end, a different sample of Ecoflex® 00-30 is cured in the rheometer itself. Both the real and the imaginary parts of the measured shear

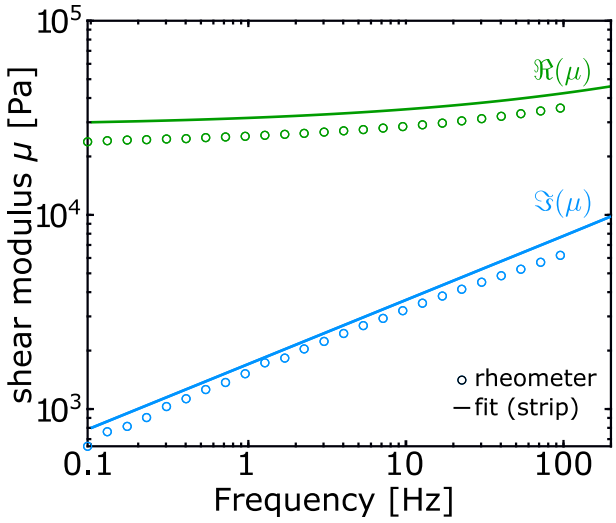


FIG. 15. **Rheology of Ecoflex®** – Measurement of the complex shear modulus of Ecoflex® in the range $0.1 - 100$ Hz with a conventional plane-plane rheometer (circles). $\Re(\mu)$ is the storage modulus of the rubber while $\Im(\mu)$ is its loss modulus. Lines correspond to the values extracted from the dispersion curves (see text).

modulus for frequencies ranging from 0.1 to 100 Hz are displayed as symbols in figure 15. In such a logarithmic scale the imaginary part of the shear modulus appears linear with a slope of almost 1/3, while the real part seems to increase slowly. Among all the available models, as the slope is not an integer it balances for a fractional derivative model. One of the simplest model which also satisfies the Kramers-Kronig relations is the fractional derivative Kelvin-Voigt model[50–52] which takes the form:

$$\mu(\omega) = \mu_0\left[1 + (\mathrm{i}\omega\tau)^n\right] \tag{25}$$

This frequency dependent complex shear modulus is injected in the Rayleigh-Lamb equation (16). Again, solving this transcendental equation is not an easy task and its roots are found with the help of an internally developed numerical Muller's algorithm. The latter

is ran with several sets of parameters of the rheological model until a satisfying agreement between theory and experiment is reached. The final set of parameters is $\mu_0 = 26$ kPa, $\tau = 260$ $\mu$s and $n = 0.33$. It almost corresponds to the measured rheology (Fig. 15) but slightly overestimates $\Re(\mu)$. This discrepancy can be attributed to temperature changes[53] or to differences (preparation or ageing) between the two samples.

The theoretical curves in figure 14 are calculated with these parameters. The wavenumber is complex and its imaginary part is rendered by the transparency of the theoretical lines. The frequency dependence of $\Re(\mu)$ induces a frequency dependence of the velocity $V_T$ which allows to fit the entire $S'_0$, $A'_0$ and $A'_1$ branches. Adding the imaginary part of the shear modulus also explains the lowered Dirac frequency. As for the absence of ZGV points, it is solely due to the viscous damping. While for a lossless material, the $S'_1$ branch and the $S'^*_{2b}$ (symmetrical to $S'_{2b}$ with respect to the $k=0$ axis) connect at the ZGV point, here, the losses separate those two branches.

## IV. GOING FURTHER

The fundamental aspects of the system have now been identified. In this section, the experiment is altered in order to investigate the role of the boundary conditions. In the Dirichlet configuration, the dispersion is found to simplify. After examining the modes polarization, selective excitation are performed by designing specific chiral sources.

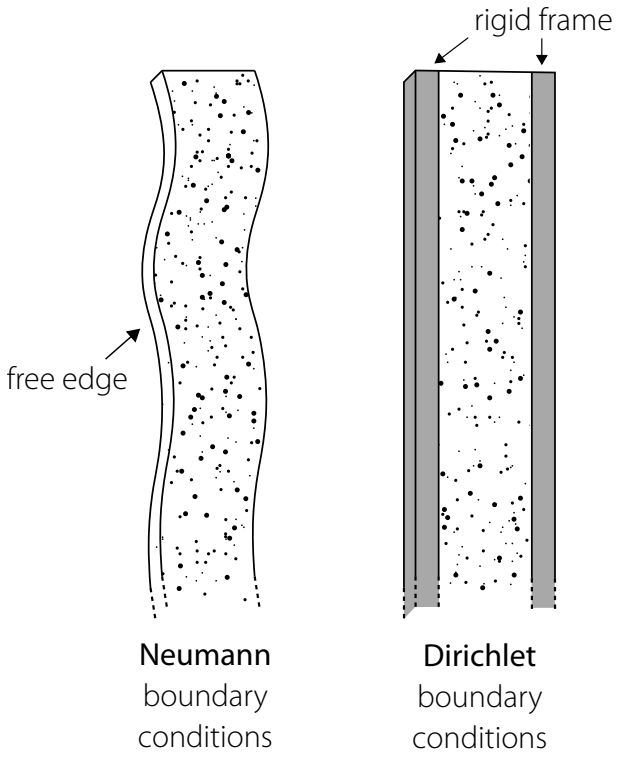


FIG. 16. **Boundary conditions** – We study the Neumann (free edges) and Dirichlet (fixed edges) boundary conditions.

### A. Investigating Dirichlet boundary conditions

In section II B 4, the analytical Lamb problem is derived assuming free boundary conditions (Neumann configuration). Here, the case of fixed boundaries (Dirichlet configuration) is investigated. In practice, these conditions can be implemented by clamping the strip in a rigid frame (Fig. 16).

#### *1. Theory*

*a. Dispersion relation.* From a theoretical point of view, switching from Neumann to Dirichlet boundaries amounts to replacing the strain cancellation condition of equations (14)

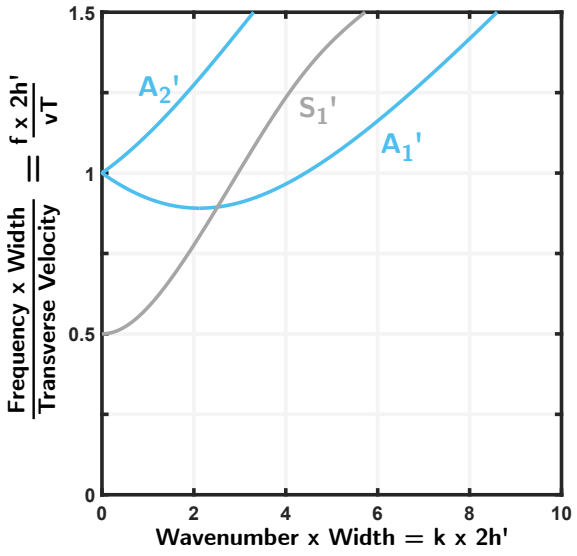


FIG. 17. **Theoretical dispersion curves of in-plane modes in a clamped soft strip** – Dispersion curves of symmetric (gray and labeled $S'$) and anti-symmetric (blue, $A'$) modes without damping. These curves evidence a Zero Group Velocity point ($A'_1$) and a backward branch, as well as a Dirac cone with a finite group velocity at $k=0$ and $f=V_T/2h'$.

by a displacement cancellation condition as follows:

$$\begin{cases} ik\phi_0 \cos(p'h'+\alpha) + q\psi_2 \cos(qh'+\alpha) &= 0 \\ -p'\phi_0 \sin(p'h'+\alpha) + ik\psi_2 \sin(qh'+\alpha) &= 0 \end{cases} \tag{26}$$

The equivalent of the Rayleigh-Lamb equation for rigid boundaries is then:

$$k^2 \sin(qh'+\alpha)\cos(p'h'+\alpha) + qp' \sin(p'h'+\alpha)\cos(qh'+\alpha) = 0 \tag{27}$$

The dispersion curves (figure 17) are obtained by searching for the roots of this equation. Compared to the Neumann case (figure 11), one important feature is the absence of propagation at low frequency ($A'_0$ and $S'_0$ have disappeared). Indeed, the rigid walls imply that no static in-plane deformation can be solution to the problem. However, the cut-off modes

474 ($A_1'$, $S_1'$, $A_2'$ *etc*) still exist. Note that the negative sloped branch, the Dirac cone and the
475 ZGV are still visible but for anti-symmetric modes rather than symmetric ones.

476 Finally, the displacements can be obtained by eliminating the coefficients $\phi_0$ and $\psi_2$ in
477 the boundary conditions of equation 26:

$$\begin{cases} u_1(x_2,\omega) = Cq\Big[\cos(p'h'+\alpha)\cos(qx_2+\alpha) \\ \qquad\qquad + \cos(qh'+\alpha)\cos(p'x_2+\alpha)\Big] \\ u_3(x_2,\omega) = -iC\Big[k\cos(p'h'+\alpha)\sin(qx_2+\alpha) \\ \qquad\qquad + p'q\cos(qh'+\alpha)\sin(p'x_2+\alpha)\Big] \end{cases} \tag{28}$$

478 Here again, the $\pi/2$ phase shift between the two components implies that the motion is
479 elliptically polarized.

480 *b. Dirac cone.* The Dirac cone appears here for the anti-symmetric modes at the same
481 frequency $f_c = V_T/2h$ as for the Neumann configuration. At this frequency, the Taylor
482 expansion of $p$ and $q$ are also given by the equation (23). These expressions are substituted
483 into the dispersion relation (27):

$$k^2 - \frac{\pi}{h'}\frac{\pi}{2h'}\frac{V_g h'}{2V_T}k\frac{V_g h'}{V_T}k = 0 \tag{29}$$

484 Leading to the same expression for the group velocity $V_g = \pm\frac{2}{\pi}V_T$.

485 Also, equation (28) provides the Taylor expansion of the displacements:

$$\begin{cases} u_1(x_2,\omega) &= -\frac{\pi}{h'}C\sin\left(\frac{\pi}{h'}x_2\right) \\ u_2(x_2,\omega) &= is\frac{\pi}{h'}C\cos\left(\frac{\pi}{2h'}x_2\right) \end{cases} \tag{30}$$

486 where $s$ indicates the sign of the group velocity. As $\cos(\pi/6) = \sin(\pi/3)$, a circular polar-
487 ization occurs for $x_2 = \pm h'/3$ while it appears at $x_2 = \pm h'$ in the Neumann configuration.

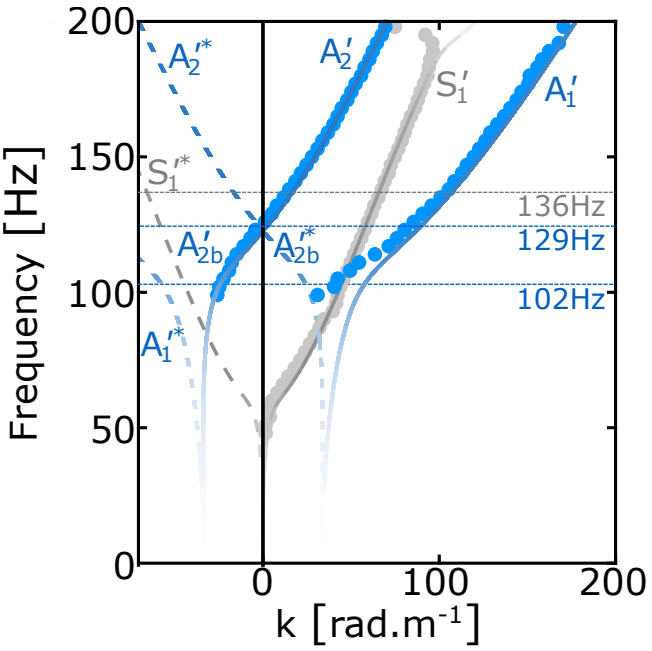


FIG. 18. **Dispersion curves of in-plane modes in the clamped strip ($2h' = 50.6$ mm)** – Experimental (symbols) and theoretical (lines) dispersion with damping (the more transparent the curve the more attenuated the mode). The $A'_2$ Dirac cone (linear crossing of the $k = 0$ axis) and the backward $A'_{2b}$ modes (negative wavenumbers) are unambiguously evidenced. The dashed lines labelled with a " * " correspond to modes propagating in the direction $-\mathbf{x_1}$ and are not measured.

### 2. *Measurements in a clamped soft strip*

*a. Dispersion.* The experiment is performed under the same conditions as before. The strip is held along its edges between two steel plates; and the separation between the edges is adjusted in order to avoid buckling or static tension. The excitation clamp is again slightly off-centered and vibrated vertically from 40 to 200 Hz. The same image analysis as in the free edges configuration allows to extract the experimental dispersion curves represented as symbols in figure 18. The three modes expected in the measured frequency range are

retrieved, and the same observations as in the free strip configuration can be made. First, the data points around 129 Hz show a linear crossing of the axis $k=0$ which evidences the existence of a Dirac cone for the anti-symmetric modes. Second, points measured below this cut-off frequency correspond to negative wavenumbers, which is the signature of a backward mode. Here again, the continuity of the points across the Dirac cone logically leads to attribute the backward modes to the branch $A_2'$, unlike what is indicated for the lossless medium theoretical curves (Fig. 17). This part of the curve is thus referred to as $A_{2b}'$.

Just like for the Neumann configuration, the theory provides a convincing agreement on the condition that the complex rheology of the material is taken into account. The value of $\Re(\mu)$ has an effect on the asymptotic slope of the branches. The value of $\Im(\mu)$ affects the Dirac frequency. In addition, the ZGV point is accurately defined only when $\Im(\mu) = 0$. In this lossy material, two modes with almost opposite wavenumbers coexist, which corresponds to a quasi ZGV point. The absence of actual ZGV point is evidenced by the disconnection between branches $A_1'$ and $A_{2b}'^*$. This is a direct consequence of the increase in losses near this point as rendered by the transparency of the lines.

*b. Tracking the displacement at the Dirac point.* Shaking the strip at 129 Hz (Dirac frequency), the in-plane motion over a complete period was extracted for 25 positions regularly spaced across the strip and located at a distance $x_1=18$ cm from the source (far enough to avoid evanescent contributions). After removing the symmetric contribution and specifically selecting the $A_2'$ mode thanks to the SVD algorithm, one can reconstruct the full trajectories as shown in figure 19a. They appear to be essentially elliptical and nearly circular at the location $x_2=\pm h'/3$ (red dashed lines) which is in agreement with equation (30).

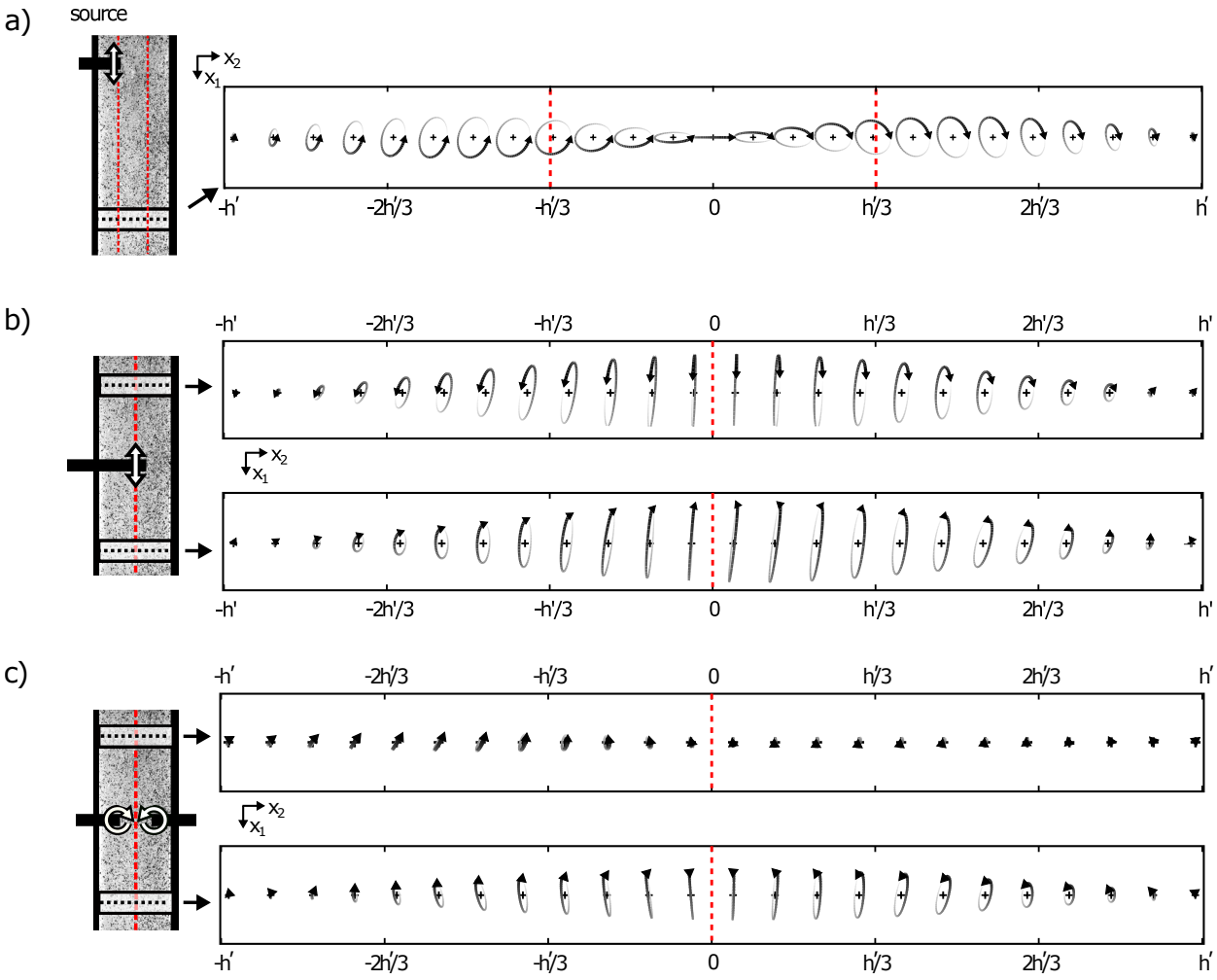


FIG. 19. **Trajectories** – From the instantaneous motion, one can reconstruct the trajectory of a solid element over a full wave period. Here, we specifically display the trajectories of elements distributed along the width of the strip at a distance $x_1 = 18$ cm (a), $\pm 10.5$ cm (b and c) from the source. The motion is magnified by a factor 80 (a), 130 (b) and 180 (c). (a) The SVD allows to separate the $A_2$ contribution and retrieve the displacement at the Dirac cone (at 129 Hz): a circular motion at positions $\pm h/3$ is observed. (b) For a symmetrical input (at 136 Hz), only the symmetrical mode $S_1$ and its reciprocal counterpart $S_1^*$ which propagates in the opposite direction are fed. (c) A chiral excitation, *i.e.* two sources placed at roughly $\pm 2h/3$ and driven circularly in a symmetric manner, permits to only feed $S_1$ and no displacement is measured on the top.

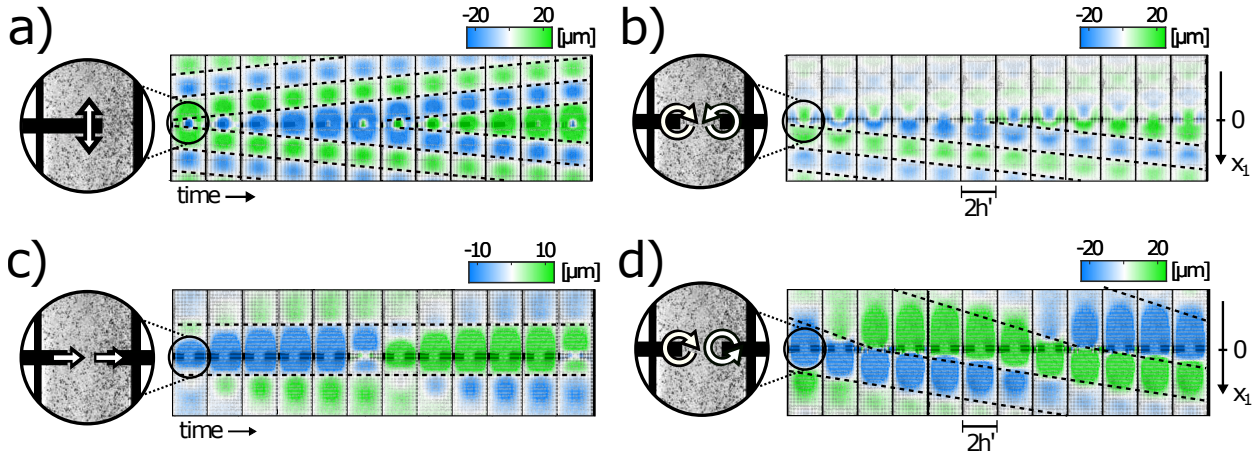


FIG. 20. **Selective excitation at 136 Hz (a and b) and 102 Hz (c and d)** – *Figure reproduced from ref* [1]. The strip is excited in a symmetrical manner (a and b) and in an anti-symmetrical manner (c and d). The black dashed lines are visual guides highlighting the zeroes of displacement and the sketches indicate the source geometry and motion. For the sake of clarity, only $u_1$ (a and b) or $u_2$ (c and d) is reported here. (a) Linear excitation. The source is placed in the centre of the strip and shaken vertically: $S_1$ and $S_1^*$ are excited and respectively travel to the bottom and the top of the strip. (b) Chiral excitation. Two sources facing each other are rotated in a symmetrical way directions: the energy is directed toward the bottom, meaning that $S_1$ is selected. (c) Linear excitation. Two sources are shaken horizontally: a stationary wave is observed. This is the signature of the quasi ZGV mode. (d) The two sources are rotated and the wave is propagative. The phase velocity is negative in the top region ($x_1 < 0$) and positive in the bottom region ($x_1 > 0$).

### B. Selective excitation

*a. One way excitation.* In the previous paragraph, the $A_2'$ mode can be isolated during the post-processing stage (thanks to the SVD). Here, the selection is directly performed during the generation stage. Curie's principle states that the resulting wavefield should at

521 least have the same symmetries as the source. As a consequence, a vertically driven source
522 placed in the middle of the strip only feeds the symmetrical modes. The displacements over
523 one cycle for such an excitation at 136 Hz are represented in figure 19b. The only available
524 symmetrical modes at 136 Hz is $S_1'$ for the bottom part and $S_1'^*$ for the top one. The motion
525 is vertical in the center while it remains elliptical everywhere else as a consequence of the $\pi/2$
526 phase shift between the two components (Equations (28)). However, the rotation directions
527 are different on either side of the source. This is consistent with the fact that $S_1'$ and $S_1'^*$
528 are phase-conjugate partners.

529 In order to exploit this specific polarization, the single vertical source is now replaced by
530 two chiral sources (see figure 19c) which are rotated in a symmetric fashion. The rotating
531 sources are designed by connecting a clamp to two perpendicular speakers, and the phase
532 quadrature excitation is controlled thanks to a 4 channels soundboard (Presonus Audiobox
533 44VSL). The resulting trajectories (figure 19c) demonstrate that $S_1'$ is fed but not $S_1'^*$: the
534 top part of the strip remains still. Indeed the rotation direction of the source corresponds to
535 that of $S_1'$; it demonstrates how chirality can be used to perform selective excitation. One
536 can get a clearer picture of the phenomenon by examining the field maps. The 12 successive
537 snapshots of the strip over a full wave period are represented next to each other in figure 20.
538 The color scale here only indicates the displacement $u_1$. Just like for figure 19b, when the
539 excitation is purely vertical, $S_1'$ and $S_1'^*$ are fed and the whole strip is excited (Fig. 20a). As
540 the source becomes chiral, only $S_1'$ is selected: waves travel in the bottom part, while the
541 top part is not excited (Fig. 20b).

542 *b. Mode separation.* Chiral selection can also be performed with anti-symmetric modes.
543 The strip is now shaken horizontally by two clamps driven simultaneously at 102 Hz (near
544 the quasi ZGV frequency) following an anti-symmetric scheme. The field pattern in fig-
545 ure 20c (which here corresponds to the displacement $u_2$) reveals stationary: the zeroes of
546 displacement remain at the same position over a full excitation period (dashed lines). This
547 is possible only if two waves propagating in opposite directions interfere on both sides of
548 the strip. According to figure 18, at this frequency, there are precisely two coexisting modes
549 on either side of the strip: $A'_1$ and $A'_{2b}$ on the bottom part, and $A'^*_1$ and $A'^*_{2b}$ on the top
550 part. Near the quasi ZGV point, their wavenumber magnitudes become similar, meaning
551 that their interferences can give birth to a standing wave.

552 As depicted in figure 20d, when the clamps are rotated in an anti-symmetrical manner,
553 the wavefield returns to propagative on both parts. And notably, the zeroes travel toward
554 the bottom on both sides (dashed lines). On the upper part, the wave-fronts are backward,
555 *i.e.* they move toward the source, and therefore corresponds to $A'^*_{2b}$. In the bottom part,
556 only $A'_1$ is fed and the wave-fronts travel away from the source. The chiral excitation has
557 allowed here to separate the two components of a quasi ZGV point.

## 558 V. CONCLUSION

559 This article introduces a new "playground" to study wave guiding of elastic waves. It
560 relies on the use of a commercial silicon elastomer. Soft elastomers enable large displacements
561 and slow propagation, which drastically facilitates the experimental procedure. With a few
562 different configurations, we show how this highly visual tool is adequate to explore wave

physics phenomena. Furthermore, their quasi-incompressible nature enables the observation of original dispersion effects such as a Dirac cone[1]. Starting with simple experiments of linearly polarized plane-waves propagating in a thin plate, it ends with complex chiral mode selection near a quasi zero-group velocity mode in a strip with clamped edges. This allows to go over the simple theory of a scalar field guided by two interfaces, namely *SH* modes, to more complex waveguides where two waves with different velocities and polarizations are coupled at each reflection, namely Lamb modes.

The work is not over and many other complex guiding geometries can be envisioned. The nearly incompressible nature of the medium being a property shared with most of the biological tissues, analogies with elastic waves existing in the living world can be made. At least three types of wave guides can be identified in the human body. The cochlear wave inside the inner ear of mammalians is supported by the basilar membrane which resembles the clamped strip studied here. The vocal cords, whose vibrations are responsible of sound control, could be the support of complex stationary fields. Last, arteries or neuronal axons are fluid filled circular soft waveguides also hosting interesting wave phenomena.

## ACKNOWLEDGMENTS

This research is supported by LABEX WIFI (Laboratory of Excellence within the French Program "Investments for the Future") under references ANR-10-LABX-24 and ANR-10-IDEX-0001-02 PSL*, and by Agence Nationale de la Recherche under reference ANR-16-CE31-0015. A.D. acknowledges funding from French Direction Générale de l'Armement.

583 **REFERENCES**

584 [1]M. Lanoy, F. Lemoult, A. Eddi, and C. Prada, "Dirac cones and chiral selection of elastic
585 waves in a soft strip," Proc Natl Acad Sci USA **117**(48), 30186–30190 (2020) doi: 10.
586 1073/pnas.2010812117.

587 [2]I. Levental, P. C. Georges, and P. A. Janmey, "Soft biological materials and their impact
588 on cell function," Soft Matter **3**(3), 299–306 (2007).

589 [3]M. A. Wozniak and C. S. Chen, "Mechanotransduction in development: a growing role for
590 contractility," Nature reviews Molecular cell biology **10**(1), 34 (2009).

591 [4]S. Kumar and V. M. Weaver, "Mechanics, malignancy, and metastasis: the force journey
592 of a tumor cell," Cancer and Metastasis Reviews **28**(1-2), 113–127 (2009).

593 [5]P. Kalita and R. Schaefer, "Mechanical models of artery walls," Archives of Computational
594 Methods in Engineering **15**(1), 1–36 (2008).

595 [6]P. R. Murray and S. L. Thomson, "Synthetic, multi-layer, self-oscillating vocal fold model
596 fabrication," JoVE (Journal of Visualized Experiments) (58), e3498 (2011).

597 [7]C. Vannelli, J. Moore, J. McLeod, D. Ceh, and T. Peters, "Dynamic heart phantom with
598 functional mitral and aortic valves," in *Medical Imaging 2015: Image-Guided Procedures,*
599 *Robotic Interventions, and Modeling*, International Society for Optics and Photonics (2015),
600 Vol. 9415, p. 941503.

601 [8]G. R. Gossweiler, C. L. Brown, G. B. Hewage, E. Sapiro-Gheiler, W. J. Trautman, G. W.
602 Welshofer, and S. L. Craig, "Mechanochemically Active Soft Robots," ACS Appl. Mater.
603 Interfaces **7**(40), 22431–22435 (2015) doi: 10.1021/acsami.5b06440.

[9]L. Marechal, P. Balland, L. Lindenroth, F. Petrou, C. Kontovounisios, and F. Bello, "Toward a common framework and database of materials for soft robotics," Soft Robotics **8**(3), 284–297 (2021).

[10]E. Siéfert, E. Reyssat, J. Bico, and B. Roman, "Bio-inspired pneumatic shape-morphing elastomers," Nature Mater **18**(1), 24–28 (2019) doi: 10.1038/s41563-018-0219-x.

[11]S. Y. Kim, R. Baines, J. Booth, N. Vasios, K. Bertoldi, and R. Kramer-Bottiglio, "Reconfigurable soft body trajectories using unidirectionally stretchable composite laminae," Nat Commun **10**(1), 3464 (2019) doi: 10.1038/s41467-019-11294-7.

[12]L. Sandrin, M. Tanter, J.-L. Gennisson, S. Catheline, and M. Fink, "Shear elasticity probe for soft tissues with 1-d transient elastography," IEEE transactions on ultrasonics, ferroelectrics, and frequency control **49**(4), 436–446 (2002).

[13]J. Foucher, E. Chanteloup, J. Vergniol, L. Castera, B. Le Bail, X. Adhoute, J. Bertet, P. Couzigou, and V. de Ledinghen, "Diagnosis of cirrhosis by transient elastography (fibroscan): a prospective study," Gut **55**(3), 403–408 (2006).

[14]J.-L. Gennisson, T. Deffieux, M. Fink, and M. Tanter, "Ultrasound elastography: principles and techniques," Diagnostic and interventional imaging **94**(5), 487–495 (2013).

[15]M. Couade, M. Pernot, C. Prada, E. Messas, J. Emmerich, P. Bruneval, A. Criton, M. Fink, and M. Tanter, "Quantitative assessment of arterial wall biomechanical properties using shear wave imaging," Ultrasound in medicine & biology **36**(10), 1662–1676 (2010).

[16]A. V. Astaneh, M. W. Urban, W. Aquino, J. F. Greenleaf, and M. N. Guddati, "Arterial waveguide model for shear wave elastography: implementation and in vitro validation,"

Physics in Medicine & Biology **62**(13), 5473 (2017).

[17]E. Maksuti, F. Bini, S. Fiorentini, G. Blasi, M. W. Urban, F. Marinozzi, and M. Larsson, "Influence of wall thickness and diameter on arterial shear wave elastography: a phantom and finite element study," Physics in Medicine & Biology **62**(7), 2694 (2017).

[18]I. Z. Nenadic, M. W. Urban, S. A. Mitchell, and J. F. Greenleaf, "Lamb wave dispersion ultrasound vibrometry (lduv) method for quantifying mechanical properties of viscoelastic solids," Physics in Medicine & Biology **56**(7), 2245 (2011).

[19]I. Z. Nenadic, M. W. Urban, S. Aristizabal, S. A. Mitchell, T. C. Humphrey, and J. F. Greenleaf, "On lamb and rayleigh wave convergence in viscoelastic tissues," Physics in Medicine & Biology **56**(20), 6723 (2011).

[20]J. Brum, M. Bernal, J. Gennisson, and M. Tanter, "In vivo evaluation of the elastic anisotropy of the human achilles tendon using shear wave dispersion analysis," Physics in Medicine & Biology **59**(3), 505 (2014).

[21]H.-C. Liou, F. Sabba, A. I. Packman, G. Wells, and O. Balogun, "Nondestructive characterization of soft materials and biofilms by measurement of guided elastic wave propagation using optical coherence elastography," Soft matter **15**(4), 575–586 (2019).

[22]J. Griesbauer, S. Bössinger, A. Wixforth, and M. F. Schneider, "Propagation of 2d pressure pulses in lipid monolayers and its possible implications for biology," Phys. Rev. Lett. **108**, 198103 (2012) doi: 10.1103/PhysRevLett.108.198103.

[23]M. Hirano, "Morphological structure of the vocal cord as a vibrator and its variations," Folia Phoniatrica et Logopaedica **26**(2), 89–94 (1974).

[24]L. Robles and M. A. Ruggero, "Mechanics of the mammalian cochlea," Physiological reviews **81**(3), 1305–1352 (2001).

[25]T. Reichenbach and A. Hudspeth, "The physics of hearing: fluid mechanics and the active process of the inner ear," Reports on Progress in Physics **77**(7), 076601 (2014).

[26]D. Royer and E. Dieulesaint, *Elastic waves in solids I: Free and guided propagation* (Springer Science & Business Media, 1999).

[27]D. N. Alleyne and P. Cawley, "The interaction of lamb waves with defects," IEEE transactions on ultrasonics, ferroelectrics, and frequency control **39**(3), 381–397 (1992).

[28]Z. Su, L. Ye, and Y. Lu, "Guided lamb waves for identification of damage in composite structures: A review," Journal of sound and vibration **295**(3-5), 753–780 (2006).

[29]S. Bramhavar, C. Prada, A. A. Maznev, A. G. Every, T. B. Norris, and T. W. Murray, "Negative refraction and focusing of elastic lamb waves at an interface," Physical Review B **83**(1), 014106 (2011).

[30]F. D. Philippe, T. W. Murray, and C. Prada, "Focusing on plates: controlling guided waves using negative refraction," Scientific reports **5**, 11112 (2015).

[31]I. Tolstoy and E. Usdin, "Wave propagation in elastic plates: low and high mode dispersion," The Journal of the Acoustical Society of America **29**(1), 37–42 (1957).

[32]S. D. Holland and D. E. Chimenti, "Air-coupled acoustic imaging with zero-group-velocity lamb modes," Applied physics letters **83**(13), 2704–2706 (2003).

[33]C. Prada, O. Balogun, and T. Murray, "Laser-based ultrasonic generation and detection of zero-group velocity lamb waves in thin plates," Applied Physics Letters **87**(19), 194109

(2005).

[34]C. Prada, D. Clorennec, and D. Royer, "Local vibration of an elastic plate and zero-group velocity lamb modes," The Journal of the Acoustical Society of America **124**(1), 203–212 (2008).

[35]S. Wildeman, "Real-time quantitative schlieren imaging by fast fourier demodulation of a checkered backdrop," Experiments in Fluids **59**(6), 97 (2018).

[36]S. Wildeman (2021), https://github.com/swildeman/dicflow.

[37]B. A. Auld, *Acoustic Fields and Waves in Solids* (John Wiley & Sons Inc., 1973).

[38]In the polymer or rheology communities the Lamé coefficient $\mu$ is noted $G$.

[39]D. E. Muller, "A method for solving algebraic equations using an automatic computer," Mathematics of Computation **10**, 208–215 (1956).

[40]A. A. Krushynska and V. V. Meleshko, "Normal waves in elastic bars of rectangular cross section," The Journal of the Acoustical Society of America **129**(3), 1324–1335 (2011) doi: 10.1121/1.3531800.

[41]M. Cross and R. Lifshitz, "Elastic wave transmission at an abrupt junction in a thin plate with application to heat transport and vibrations in mesoscopic systems," Physical Review B **64**, 085324 (2001) doi: 10.1103/PhysRevB.64.085324.

[42]J. Laurent, D. Royer, and C. Prada, "In-plane backward and zero-group-velocity guided modes in rigid and soft strips," The Journal of the Acoustical Society of America **147** (2020) doi: 10.1121/10.0000760.

[43]R. D. Mindlin, *An Introduction to the Mathematical Theory of Vibrations of Elastic Plates* (J. Yang (Ed.),, World Scientific, Singapore, 2006).

[44]D. M. Stobbe and T. W. Murray, "Conical dispersion of lamb waves in elastic plates," Physical Review B **96**(14), 144101 (2017).

[45]A. Maznev, "Dirac cone dispersion of acoustic waves in plates without phononic crystals," The Journal of the Acoustical Society of America **135**(2), 577–580 (2014).

[46]X. Huang, Y. Lai, Z. H. Hang, H. Zheng, and C. Chan, "Dirac cones induced by accidental degeneracy in photonic crystals and zero-refractive-index materials," Nature materials **10**(8), 582 (2011).

[47]R. D. Mindlin and M. A. Medick, "Extensional Vibrations of Elastic Plates," Journal of Applied Mechanics **26**(4), 561–569 (2021) doi: 10.1115/1.4012112.

[48]B. Gérardin, J. Laurent, C. Prada, and A. Aubry, "Negative reflection of lamb waves at a free edge: Tunable focusing and mimicking phase conjugation," The Journal of the Acoustical Society of America **140**(1), 591–600 (2016).

[49]Again, in the polymer or rheology communities the Lamé coefficient $\mu$ is noted $G$ which leads to the real part $G'$ and the imaginary part $G''$.

[50]F. C. Meral, T. J. Royston, and R. L. Magin, "Surface response of a fractional order viscoelastic halfspace to surface and subsurface sources," The Journal of the Acoustical Society of America **126**(6), 3278–3285 (2009).

[51]S. P. Kearney, A. Khan, Z. Dai, and T. J. Royston, "Dynamic viscoelastic models of human skin using optical elastography," Physics in Medicine & Biology **60**(17), 6975 (2015).

[52]E. Rolley, J. H. Snoeijer, and B. Andreotti, "A flexible rheometer design to measure the visco-elastic response of soft solids over a wide range of frequency," Review of scientific instruments **90**(2), 023906 (2019).

[53]Y. Wan, Y. Xiong, and S. Zhang, "Temperature dependent dynamic mechanical properties of magnetorheological elastomers: Experiment and modeling," Composite Structures **202**, 768–773 (2018).

## REFERENCES

[1]In the polymer or rheology communities the Lamé coefficient $\mu$ is noted $G$.

[2]Again, in the polymer or rheology communities the Lamé coefficient $\mu$ is noted $G$ which leads to the real part $G'$ and the imaginary part $G''$.